Experimental and Theoretical Characterization of the Optical Properties of CeO_2, $SrCeO_3$, and Sr_2CeO_4 Containing Ce^{4+} (f^0) Ions

Fabrice Goubin,[†] Xavier Rocquefelte,[†] Myung-Hwan Whangbo,[‡] Yvan Montardi,[§] Raymond Brec,[†] and Stéphane Jobic*,[†]

Institut des Matériaux Jean Rouxel, Laboratoire de Chimie des Solides, UMR 6502 CNRS-Université de Nantes, 2 rue de la Houssinière, BP 32229, 44322 Nantes Cedex 3, France, Department of Chemistry, North Carolina State University, Raleigh, North Carolina 27695-8204, and Rhodia Electronics & Catalysis, 52 rue de la Haie Coq, 93308 Aubervilliers, France

Received July 11, 2003. Revised Manuscript Received November 3, 2003

In an effort to find new UV absorbers, the optical properties of CeO_2, $SrCeO_3$, and Sr_2CeO_4 were examined by UV−visible diffuse reflectance measurements and electron energy-loss spectroscopy (EELS), and their electronic structures were investigated on the basis of first-principles density functional theory (DFT) calculations. The extinction coefficient k and the refractive index n determined from the loss function $Im(-1/\epsilon)$ by EELS were compared with the corresponding quantities calculated from DFT calculations. The UV absorption thresholds of these materials were determined by the electron excitation from the O 2p anionic band to the empty Ce 4f orbitals. The calculated and measured refractive indices were in satisfactory agreement. The applicability of CeO_2, $SrCeO_3$, and Sr_2CeO_4 as potential UV absorbers was assessed.

Introduction

The UV part of the solar spectrum reaching the earth surface is divided into two domains, UVA (320−400 nm, i.e., 3.10−3.87 eV) and UVB (280−320 nm, i.e., 3.87−4.43 eV), which are responsible for suntans and sunburns, respectively. The link between UVB exposure and skin cancers is now well-established. Due to the lower energy, UVA causes less local damages than does UVB, but penetrates deeper in the skin. It has been shown that the long-term harmful effects of UVA are not negligible, particularly for skin aging and cancer.[1] Consequently, there is a strong need for UVA and UVB protection, which is partially met by combining several organic ultraviolet filters.[2] Unfortunately, mixed organic compounds possess undesirable problems in terms of industrial use and health compatibility. For this reason, and also owing to the need to minimize exposure to organic chemicals, inorganic UV shields attract much attention. Practically, zinc and titanium oxides account for almost all sunscreen particles used today. Actually, this stems more from the existing manufacturing know-how rather than from the real intrinsic optical properties of these minerals, which are best used as white pigments.

For most purposes, sunscreen compounds must have as little color and opacity as possible. This means that they should absorb poorly in the visible range of the solar spectrum, and their refractive index should be similar to that of the medium in which they are dispersed. Then, the sunscreen particle will appear invisible, and the light will not be altered as it goes from medium to particle and back to medium. These two properties are a matter of aesthetics because, besides the performance of an inorganic sunscreen to absorb in the UV region, whitening should be minimal. To fulfill this need, transparent grades of both TiO_2 and ZnO [3] have been developed. These insulating materials are specifically designed to attenuate the UVB and UVA portions of the electromagnetic spectrum while minimizing interactions with the visible portion. This change in the optical properties of these materials is achieved purely by modifying their mean particle size, not changing the chemical structure of the materials. Hence, manufactured with a powder size ranging from 80 to 150 nm, the zinc oxide (n = 2.01−2.03, energy gap of 3.06 eV) efficiently absorbs radiation over virtually the whole UV region (380 nm and shorter). In contrast, titanium oxide (n = 2.75 for the rutile form, energy gap of 3.23 eV) [4,5] turns out to be predominately a very efficient UVB absorber but a UVA scatterer. Bigger and

* Corresponding author. E-mail: Jobic@cnrs-imn.fr. Tel.: (33) 02 40 37 39 22.
[†] Institut des Matériaux Jean Rouxel.
[‡] North Carolina State University.
[§] Rhodia Electronics and Catalysis.

(1) Pathak, M. A. In *Sunscreens: Development, evaluation, and regulatory aspects*, 2nd ed.; Lowe, N. J., Shaath, N. A., Pathak, M. A., Eds.; Marcel Dekker, Inc.: Phoenix, 1997; Vol. 15, p 59.

(2) Janousek, A. In *Sunscreens: Development, evaluation, and regulatory aspects*, 2nd ed.; Lowe, N. J., Shaath, N. A., Pathak, M. A., Eds.; Marcel Dekker, Inc.: Phoenix, 1997; Vol. 15, p 215.

(3) Fairhurst, D.; Mitchnick, M. A. In *Sunscreens: Development, evaluation, and regulatory aspects*, 2nd ed.; Lowe, N. J., Shaath, N. A., Pathak, M. A., Eds.; Marcel Dekker, Inc.: Phoenix, 1997; Vol. 15, p 313.

(4) Shionoya, S., Yen, W. M., Eds. *Phosphor Handbook*, CRC Press: Boca Raton, FL, 1999.

(5) Lide, D. R., Ed. *Hanbook of chemistry and physics*, 93rd ed.; CRC Press: Boca Raton, FL, 2003.

10.1021/cm034618u CCC: $27.50
Published on Web 01/28/2004

whiter TiO_2 particles are better as a UVA absorber, but have poorer aesthetics properties.

Ceria CeO_2 has a band gap of 3.2 eV and a high UV absorption and a refractive index of 2.35. It has been patented for its gas-converting properties[6,7] and has been proposed as a potential substitute for TiO_2. In contrast to rutile TiO_2 and ZnO, ceria exhibits a much lower photocatalytic activity[8] and hence limits the formation of reactive oxygen species, thus reducing the degradation of the medium containing the UV absorber particles. Nevertheless, the catalytic activity of ceria for the oxidation of organic materials is well-known,[9] so silica coating is necessary for any industrial application of CeO_2 as a UV absorber. However, this problem can be partially solved by doping ceria with zinc oxide or calcium oxide without degrading the intrinsic properties of CeO_2.[10]

The aim of the present work is to examine the electronic structures of the Ce^{4+}-containing oxides CeO_2, $SrCeO_3$, and Sr_2CeO_4 and probe the role of their 4f orbitals in the optical properties, that is, the optical gap and the refractive index. The nature of the O 2p−Ce 4f charge transfer has already been evidenced for CeO_2,[11,12] but there has been no report concerning the refractive index n. We focus our attention on the trends in the optical properties and electronic band structures of CeO_2, $SrCeO_3$, and Sr_2CeO_4.

Experimental Section

Synthesis. Samples of white CeO_2 used for our physical property measurements, that is, UV/visible spectroscopy and electron energy loss spectroscopy (EELS), or used as precursors in the preparation of Sr_2CeO_4 and $SrCeO_3$ were supplied by Rhodia Electronic & Catalysis (99.99%). The synthetic route used for the preparation of Sr_2CeO_4 and $SrCeO_3$ was similar to that reported in the literature.[13] Sr_2CeO_4 was prepared from the reaction of the mixture of $SrCO_3$ (Prolabo, 99%) and CeO_2 in the 1.1:2.0 mole ratio in air at 1000 °C for 60 h with three intermediate re-grindings. A similar procedure was used for the preparation of $SrCeO_3$, using the precursors $SrCO_3$ and CeO_2 in the 2.2:1 mole ratio. $SrCeO_3$ is obtained as a light brown powder in the first firing, and the color is due probably to the presence of Ce^{3+} (associated with a slight nonstoichiometry in oxygen). A final firing at 1000 °C for 60 h in a pure O_2 atmosphere yielded a white-cream pure powder. The purity of the final products was systematically checked by means of Rietveld analysis[14] of the X-ray patterns collected on a Siemens D5000 diffractometer (Cu K-$L_{3,2}$, $\lambda = 1.540598$ and 1.544390 Å; reflection geometry; linear detector with a 0.18°/min sweep speed; digitization with a 0.03° step). No impurity was detected even after a long X-ray exposure. SEM measurements for CeO_2, Sr_2CeO_4, and $SrCeO_3$ were performed with a JEOL JSM-5800LV microscope coupled with a germanium PGT Prism detector.

Optical Spectroscopy. The UV−visible diffuse reflectance spectra were recorded with a Perkin-Elmer Lambda 900 spectrometer with 0.1-nm resolution. This instrument was equipped with a 150-mm-diameter Labsphere integrating sphere and was computer-controlled using the UV winlab software. The reflectance vs wavelength measurements were made in the 240−620 nm range (i.e., 2−5.17 eV) with a Spectralon sample as reference (100% reflectance). To cut Sr_2CeO_4 blue fluorescence, the high-energy part of the spectrum ($E > 3.2$ eV) was recorded with a filter absorbing in the emission range (400−650 nm) of the compound. The absorption (K/S) data were calculated from the reflectance spectra using the Kubelka−Munk function, $K/S = (1 - R)^2/2R$, where $R(\lambda)$, $K(\lambda)$, and $S(\lambda)$ are the reflectance, the absorption coefficient, and the scattering coefficient, respectively. For particles with average diameter d greater than twice the wavelength λ (i.e., $d > 0.8\ \mu$m in the UV range), $S(\lambda)$ is a parameter independent of wavelength but dependent on the grain size d. In practice, and under this experimental restriction, the diffuse reflectance increases as the particle size increases, but the position of the absorption threshold remains identical for all grain sizes.[15] Since measurements were carried out on samples with a particle size ranging from 1 to 5 μm, as checked by SEM, the absorption threshold could be taken as the intersection point between the energy axis and the line extrapolated from the linear portion of the absorption edge in the K/S vs E plot. The optical properties n and k cannot be straightforwardly deduced from diffuse reflectance measurements.[16]

Electron Energy Loss Spectroscopy. EELS characterization of powder samples was carried out using a transmission electron microscope (TEM) Philips CM 30 equipped with a LaB_6 gun, coupled with a GATAN 666 spectrometer controlled by the ELP3 software. EELS was used to deduce the optical constants of the powder samples. The TEM was operated at 100 kV, with an unsaturated beam, to optimize the spectral resolution. A fwhm of 0.8 eV is routinely achieved in these conditions. We used the image coupling mode, in which the diffraction pattern is sent in the aperture of the spectrometer using the following parameters: entrance aperture diameter of 2 mm, energy dispersion of 0.1 eV, and acquisition time below 500 ms. Acquisition of spectra was made in the nanoprobe mode in a 10−20 nm area. An electron diffraction pattern was used qualitatively to select a thin area and avoid crystals that have one of their crystallographic axes oriented along the electron beam. The convergence angle (3.5 mrad) was high enough to make the analysis independent of orientation. Eight spectra were acquired in the 0−80 eV energy range, aligned and summed together. Acquisition and comparison of spectra translated on the photodiode array made it possible to ensure that low-intensity features on the spectra in the energy range 2−5 eV were not due to a "ghost" or remnant effect after exposing the photodiode array with zero loss high-intensity peak, to which a GATAN 666 spectrometer is sensitive.

The four-step mathematical treatment of EELS spectra, already reported elsewhere,[17,18] leads to a proper determination of the energy-dependent loss function $Im(-1/\epsilon)$, where ϵ is the complex dielectric function. The real part of $1/\epsilon$ was then calculated from the imaginary part using the Kramers−Kronig relation

$$Re\left(\frac{1}{\epsilon(E)}\right) = 1 - \frac{2}{\pi} P \int_0^\infty Im\left(\frac{-1}{\epsilon(E)}\right) \frac{E'}{E'^2 - E^2}\, dE' \qquad (1)$$

where P refers to the principal part of the Cauchy integral. The real ϵ_1 and the complex ϵ_2 part of the dielectric function ϵ were deduced from $Im(-1/\epsilon)$ and $Re(1/\epsilon)$ using the formulas

(6) Rhodia: WO 00/49098, 2000.
(7) Rhone-Poulenc: US5626826, 1997.
(8) Miyauchi, M.; Nakajima, A.; Watanabe, T.; Hashimoto, K. *Chem. Mater.* **2002**, *14*, 2812−2816.
(9) Primet, M.; Garbowski, E. In *Catalysts by Ceria and Related Materials*; Trovarelli, A., Ed.; Imperial College Press: London, 2002; p 407.
(10) Yabe, S.; Yamashita, M.; Shigeyosi, M.; Kazuyuki, T.; Yoshida, S.; Li, R.; Sato, T. *Int. J. Inorg. Mater.* **2001**, *3*, 1003−1008.
(11) Skorodumova, N. V.; Ahuja, R.; Simak, I.; Abrikosov, I. A.; Johansson, B.; Lundqvist, B. I. *Phys. Rev. B* **2001**, *64*, 115108−115101 115108−115109.
(12) Marabelli, F.; Wachter, P. *Phys. Rev. B* **1987**, *36*, 1238−1243.
(13) van Pieterson, L.; Soverna, S.; Meijerink, A. *J. Electrochem Soc.* **2000**, *147*, 4688−4691.
(14) Rietveld, H. M. *J. Appl. Crystallogr.* **1969**, *2*, 65−71.
(15) Cervelle, B.; Bédidi, A.; Flay, N. *Photo-Interprét.* **1996**, *2*.
(16) Kortüm, G. *Reflectance Spectroscopy*; Springer-Verlag: New York, 1969.
(17) Egerton, R. F. *Electron energy loss spectroscopy in the electron microscope*; Plenum Press: New York, 1986.
(18) Goubin, F.; Montardi, Y.; Deniard, P.; Rocquefelte, X.; Brec, R.; Jobic, S. *J. Solid State Chem.* **2003**, in press.

$$\epsilon_1 = Re(1/\epsilon)/[Re(1/\epsilon)^2 + Im(-1/\epsilon)^2]$$

$$\epsilon_2 = -Im(-1/\epsilon)/[Re(1/\epsilon)^2 + Im(-1/\epsilon)^2] \quad (2)$$

This leads to the refractive index n and the extinction coefficient k of the complex refractive index $N = n + ik$ on the basis of the relationships $\epsilon_1 = n^2 - k^2$ and $\epsilon_2 = 2nk$.

The normalization of $Im(-1/\epsilon)$ before the Kramers-Krönig transformation requires the knowledge of the refraction index n_0 at $E = 0$ eV (vide infra). In the case of CeO_2 we have chosen $n_0 = 2.4$. For $SrCeO_3$ and Sr_2CeO_4 we have tested different n_0 values between 2.0 and 2.3. Results here are shown for $n_0 = 2.2$. At this stage, it has to be emphasized that the n_0 value does not correspond, strictly speaking, to the refractive index reported in textbooks or databases because the latter are usually determined in the visible range. Nevertheless, the $n(E)$ curve is sufficiently flat at low energy so that n_0 can be considered as a good approximation of the refractive index.

In the case of Sr_2CeO_4, we observed by TEM that the surface of the particles was modified with the presence of strontium carbonate $SrCO_3$ in the form of small prismatic crystals. Even by careful localization of the electron probe to perform EELS measurements, to avoid these small strontium carbonate crystals, we are not entirely confident that the spectra correspond to pure and stoichiometric Sr_2CeO_4.

Theoretical Considerations

Electronic Band Structure. The full-potential linearized augmented plane wave (FP-LAPW) method implemented in the WIEN2K code[19] was used to calculate the electronic band structures and the dielectric tensors of CeO_2, Sr_2CeO_4, and $SrCeO_3$. In the LAPW method, the unit cell is divided into two types of regions, that is, the atomic spheres centered at the nuclear sites and the interstitial region between the nonoverlapping spheres. Inside the atomic spheres, the wave functions are replaced by atomic like functions while in the interspheres region the wave function of a Bloch state is expanded in plane waves. The exchange and correlation energies were treated within the density functional theory (DFT) using the Perdew-Burke-Ernzerhof generalized gradient approximation (GGA).[20] The basis set cutoff parameters were $G_{max} = 14$ and $R_{mt} \times K_{max} = 8$ (R_{mt} is the smallest atomic sphere radius in the unit cell and K_{max} is the magnitude of the largest k vector) with the muffin-tin radii of 2.4 au for Ce, 2.3 au for Sr, and 1.72 au for O. The self-consistencies were carried out on a 16, 18, and 48 k-points mesh in the irreducible Brillouin zone for CeO_2, $SrCeO_3$, and Sr_2CeO_4, respectively.

Dielectric Function. The dielectric function of an anisotropic material is a complex symmetric second-order tensor, which describes the linear response of an electronic system to an applied external electric field. The imaginary part of the dielectric tensor is directly related to the electronic band structure of a solid and can be computed using the one-electron orbitals and energies obtained by solving the Kohn−Sham equations. The underestimation of the band gap (inherent in DFT calculations)[21] was corrected by introducing a "scissors operator", which raises the bands lying above the valence bands and rescales the matrix elements.[22,23] Under the one-electron rigid band approximation, which neglects relaxation effects, and in the limit of linear optics,[24,25] the imaginary part of a matrix element of the dielectric tensor $\epsilon_{\alpha\beta}$ is given by

$$Im\ \epsilon_{\alpha\beta}(\omega) = \frac{4\pi^2 e^2}{m^2\left(\omega - \frac{\Delta_C}{\hbar}\right)^2}\sum_{i,f}\int_{BZ}\frac{2dk}{(2\pi)^3}|\langle i_k|p_\beta|f_k\rangle||\langle f_k|p_\alpha|i_k\rangle|\delta(E_f(k) + \Delta_C - E_i(k) - \hbar\omega) \quad (3)$$

for a vertical transition from a filled initial state $|i_k\rangle$ of energy $E_i(k)$ to an empty final state $|f_k\rangle$ of energy $E_f(k)$. Here, Δ_C is the shift value of the scissors operator, ω the frequency, e the electron charge, m the free electron mass, and p_α the Cartesian component of the momentum operator. The dielectric function describes a causal response, so the real and imaginary parts are linked by a Kramers−Kronig transformation. This was used to obtain the real part $\epsilon_1(\omega)$. A Lorentzian broadening of 0.05 eV was used to account for the finite life in the excited state. To obtain the isotropic dielectric function, the components of the matrix trace were averaged, that is, $\epsilon_{iso} = (\epsilon_{xx} + \epsilon_{yy} + \epsilon_{zz})/3$. The complex refractive index was calculated with the formulas given above. For dielectric tensor calculations, the BZ integration was carried out with 104, 180, and 180 independent k-points for CeO_2, $SrCeO_3$, and Sr_2CeO_4, respectively. Use of a denser k-point sampling of the BZ did not modify the dielectric tensors values.

Results and Discussion

Structural Features. The structural features of CeO_2, $SrCeO_3$, and Sr_2CeO_4 have already been reported in the literature.[26−28] CeO_2 crystallizes in the fluorite CaF_2 cubic structure type and can be regarded as consisting of CeO_8 cubes sharing each edge with an adjacent cube (Figure 1a). Alternatively, the structure can be described from OCe_4 tetrahedra sharing their edges with adjacent OCe_4 tetrahedra. $SrCeO_3$ has an orthorhombic perovskite structure with each CeO_6 octahedron sharing each corner with other CeO_6 octahedra to give rise to a three-dimensional (3D) lattice. The Sr atoms are located in tunnels (Figure 1b), while the oxygen atoms are located at the centers of distorted OCe_2Sr_2 tetrahedra and OCe_2Sr_3 square pyramids. Sr_2CeO_4 contains CeO_6 octahedra, which condense by sharing edges to form infinite CeO_4 chains separated by Sr atoms (Figure 1c). This phase has two chemical environments for oxygen atoms, OCe_2Sr_3 trigonal bi-

(19) Blaha, P.; Schwartz, K.; Madsen, G. K. H.; Kvasnicka, D.; Luiz, J.

(20) Perdew, J. P.; Burke, S.; Erzenrhof, M. *Phys. Rev. Lett.* **1996**, *77*, 3865.

(21) Sham, L. J.; Schlüter, M. *Phys. Rev. Lett.* **1983**, *51*, 1888.

(22) Puschnig, P.; Ambrosch-Draxl, C. *Phys. Rev. B* **1999**, *60*, 7891−7898.

(23) Del Sole, R.; Girlanda, R. *Phys. Rev. B* **1993**, *48*, 11789−11795.

(24) Lynch, W. D. In *Handbook of Opticals Constants of Solids*; Palik, E. D., Ed.; Academic Press: New York, 1985; p 189.

(25) Bassani, F.; Pastori Parravicini, G.; Ballinger, R. A. *Electronic states and optical transitions in solids*; Pergamon Press: New York, 1975; Vol. 8.

(26) Brauer, G.; Gradinger, H. *Z. Anorg. Allg. Chem.* **1954**, *277*, 89−95.

(27) Danielson, E.; Devenney, M.; Giaquinta, D. M.; Golden, J. H.; Haushalter, R. C.; McFarland, E. W.; Poojary, D. M.; Reaves, C. M.; Weinberg, W. H.; Wu, X. D. *J. Mol. Struct.* **1998**, *470*, 229−235.

(28) Ranlov, J.; Nielsen, K. *J. Mater. Chem.* **1994**, *4*, 867−868.

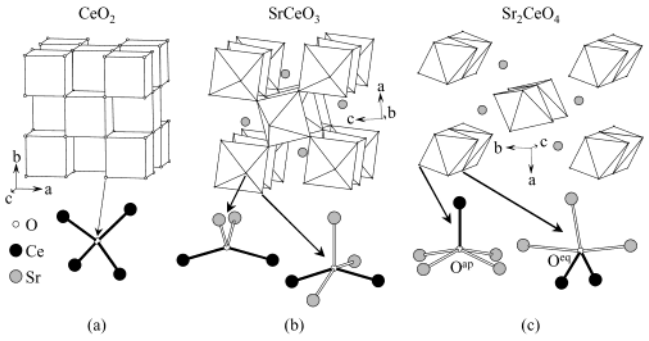

Figure 1. Schematic polyhedral representations of the crystal structures of (a) CeO_2, (b) $SrCeO_3$, and (c) Sr_2CeO_4. The oxygen atom environments are also schematically shown.

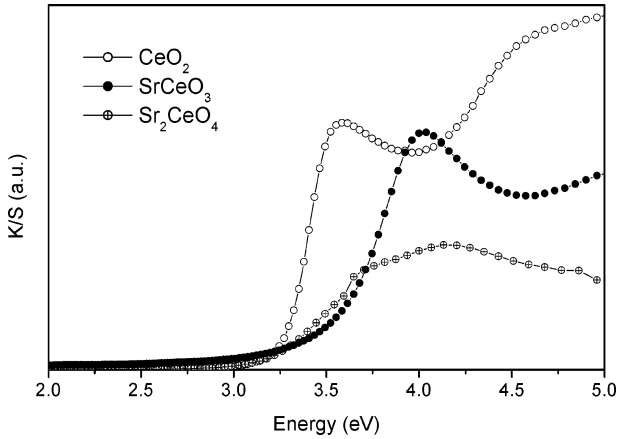

Figure 2. Kubelka−Munk function *K*/*S* versus energy *E* measured for CeO_2, $SrCeO_3$, and Sr_2CeO_4.

pyramids for equatorial oxygen (O_{eq}) and OSr_4Ce square pyramids for apical oxygen (O_{ap}).

Optical Properties. The Kubelka−Munk transformed diffuse reflectance spectra of CeO_2, $SrCeO_3$, and Sr_2CeO_4 are displayed in Figure 2. The three compounds exhibit a broad absorption band with an onset at ∼3.2, ∼3.2, and ∼3.5 eV for CeO_2, Sr_2CeO_4, and $SrCeO_3$, respectively. The steepness of the absorption around the absorption edge decreases from CeO_2 to $SrCeO_3$ and Sr_2CeO_4. In the 2.0−5.0-eV range, the absorption spectra could be distinctly grouped into two well-separated bands for CeO_2 and $SrCeO_3$, whereas only one wide band with a shoulder at low energy (∼3.6 eV) is observed for Sr_2CeO_4.

The gap value obtained for CeO_2 agrees well with ∼3 eV reported by Marabelli et al.[12] using single-crystal total reflectance spectroscopy and by Wuilloud et al.[29] using Bremsstrahlung isochromat spectroscopy and X-ray photoelectron spectroscopy on powder. Wuilloud et al.[29] suggested that the absorption originates from a charge transfer from O^{2-} to Ce^{4+}, that is, the O $2p^6 \rightarrow$ Ce $4f^0$ electronic transition (vide infra). For Sr_2CeO_4, the value of the optical gap can be derived from the excitation spectrum since its fluorescence originates from the Ce 4f → O 2p charge transfer.[13] Using the curve given by van Pieterson et al.,[13] we deduce a gap of ∼3.3 eV, in agreement with ∼3.2 eV obtained in the present work. No data were reported in the literature concerning the optical gap of $SrCeO_3$.

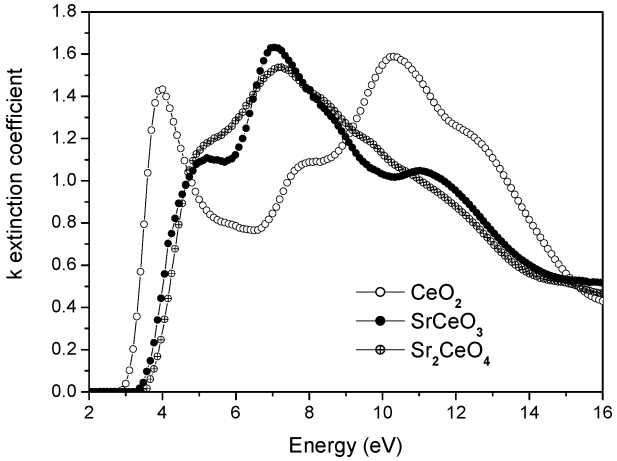

Figure 3. Extinction coefficient *k* versus energy *E* measured by EELS for CeO_2, $SrCeO_3$, and Sr_2CeO_4.

The extinction coefficients *k* vs energy curves determined for CeO_2, $SrCeO_3$, and Sr_2CeO_4 by EELS are presented in Figure 3. The spectrum of CeO_2 can be decomposed into two main absorption bands centered around 4 and 11 eV, which can be assigned to the O $2p^6 \rightarrow$ Ce $4f^0$ and O $2p^6 \rightarrow$ Ce $5d^0$ electronic transitions, respectively (vide infra). The first band ranges from 3 to 6 eV and the second one from 7 to 16 eV. The latter suggests that the Ce 5d-block bands are wide. In $SrCeO_3$ and Sr_2CeO_4, these two bands merge into one with three distinct contributions. The absorption gaps deduced from EELS agree well with those determined from diffuse reflection measurements for CeO_2 (3.15 vs 3.2 eV) and $SrCeO_3$ (3.5 vs 3.5 eV), while a difference of 0.5 eV is observed for Sr_2CeO_4 (3.7 vs 3.2 eV). As for a cause for the latter discrepancy, one might suggest a reaction of the materials surface with air (with the formation of $SrCO_3$), as already noted by Park et al.[30] However, it should influence the diffuse reflectance measurements, which agree well with the optical data reported in the literature, more strongly than the EELS results, which depend on the bulk properties of materials. Nevertheless, due to the thickness of the samples, EELS measurements on Sr_2CeO_4 were collected from the border of the grains so that the resulting electronic information may not entirely correspond to the Sr_2CeO_4 bulk. Consequently, the 3.2 eV gap from the diffuse reflectance measurements is more reliable than the 3.7 eV gap determined from EELS. It is important to note that the absorption gaps determined for CeO_2 and $SrCeO_3$ by diffuse reflectance and EELS measurements are very similar despite fundamental differences in their methodologies.

Electronic Band Structures. Figure 4 shows plots of the total density of states (DOS) for CeO_2, $SrCeO_3$, and Sr_2CeO_4 as well as those of the projected DOS for some atomic orbitals. Here, the zero energy was taken as the highest occupied energy level of CeO_2. To compare the relative positions of the energy bands of CeO_2, $SrCeO_3$, and Sr_2CeO_4, the DOS plots of the $SrCeO_3$ and Sr_2CeO_4 were given such that their Ce 1s core levels are identical to that of CeO_2.

The DOS plots of Figure 4 can be divided into three parts: (i) the valence band (VB) is of mainly the O 2p

(29) Wuilloud, E.; Delley, B.; Schneider, W.-D.; Baer, Y. *Phys. Rev. Lett.* **1984**, *53*, 202−205.

(30) Park, C. H.; Kim, C. H.; Pyun, C. H.; Choy, J. H. *J. Lumin.* **2000**, *87*−*89*, 1062−1064.

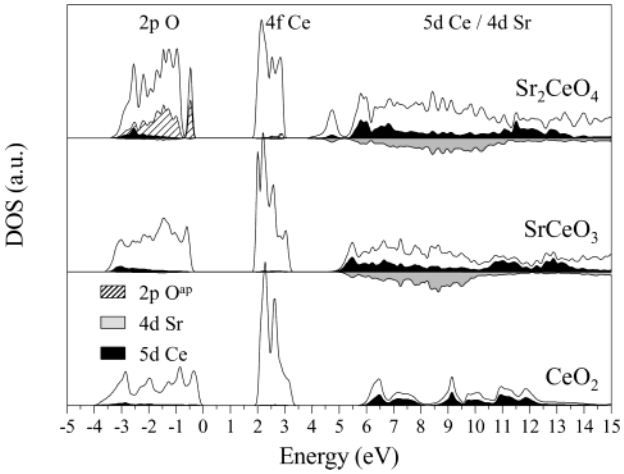

Figure 4. Total DOS plots of CeO_2, $SrCeO_3$, and Sr_2CeO_4 with the projected DOS plots for some atomic orbital contributions.

Table 1. O 2p−Ce 4f and O 2p−Ce 5d Gaps of CeO_2, $SrCeO_3$, and Sr_2CeO_4 Obtained from Diffuse Reflectance (DR) and EELS Measurements as Well as from DFT Calculations

	O 2p−Ce 4f			O 2p−Ce 5d
	DR (eV)	EELS (eV)	DFT (eV)	DFT (eV)
CeO_2	3.2	3.15	2	5.75
$SrCeO_3$	3.5	3.5	2.34	5.3
Sr_2CeO_4	3.2	3.7	2.2	4.4

orbitals in character. The width of the VB decreases from 4 to 3.26 eV to 3.13 eV on going from CeO_2 to $SrCeO_3$ and Sr_2CeO_4. The VB is slightly lower in energy for Sr_2CeO_4 and $SrCeO_3$ than for CeO_2. (ii) the conduction band (CB) of mainly the Ce 5d orbitals (as well as the Sr 4d orbitals for $SrCeO_3$ and Sr_2CeO_4) in character lies at 5.75, 5.3, and 4.4 eV above the VB for CeO_2, $SrCeO_3$, and Sr_2CeO_4, respectively. The bottom of the CB is lower as the Sr/Ce ratio increases. (iii) The Ce 4f-block band of width 1 eV lies between the VB and CB and is located at 2.0, 2.3, and 2.2 eV above the top of the O 2p-block bands in CeO_2, $SrCeO_3$, and Sr_2CeO_4, respectively. The position of the Ce 4f-block band with respect to the Ce 1s core level is almost identical for all three compounds despite the differences in their stoichiometry and Ce environments. This may be a fortuitous result or may reflect that the Ce 4f-orbitals are localized and empty.

The calculated electronic band structures make it unambiguous to assign the first absorption band of these three materials to an O^{2-} 2p → Ce^{4+} 4f charge transfer, that is, the electron excitation from the VB to the 4f-block bands. The band gap associated with this excitation determined by DFT calculations is smaller than the experimental value. This discrepancy originates from the tendency for DFT calculations to underestimate a band gap and the difficulty of properly describing localized 4f orbitals in DFT calculations. Nevertheless, the trend in the band gaps in the three oxides, that is, the increase in the optical absorption threshold on going from CeO_2 to $SrCeO_3$ and Sr_2CeO_4 is well-reproduced (see Table 1). In terms of both the DOS plot and the band gap value, our results for CeO_2 are in good agreement with those reported in previous studies.[11,31−33] In the photoemission studies of CeO_2 and $SrCeO_3$, Matsumoto et al.[34] interpreted their results by considering the ground state as the mixed valence between the $4f^0$ and $4f^1$ $\underline{L}$ configurations. This interpretation is in contradiction with the previous experiment[12] and electronic structure calculations,[11,31−33] and with the present study.

The VB−CB gap (i.e., the O 2p → Ce 5d excitation gap) is larger for CeO_2 than for $SrCeO_3$ and Sr_2CeO_4. This suggests that the Ce−O bonds have a stronger ionic character, and hence a smaller contribution of the Ce 5d and 4f orbitals in the VB, in CeO_2. Indeed, our calculations show that the contribution of the Ce 5d orbitals to the VB per Ce atomic sphere is smaller in CeO_2 than in $SrCeO_3$ to Sr_2CeO_4 by about 8.5% and 8%, respectively. Likewise, the contribution of the Ce 4f orbitals to the VB per Ce atomic sphere is smaller in CeO_2 than in $SrCeO_3$ to Sr_2CeO_4 by about 4.6% and 5%, respectively. This difference may be rationalized in terms of the inductive effect of Sr on the Ce−O bond:[35] due to the lower electronegativity of Sr compared to Ce (1.12 vs 0.95), the Ce−O bond is more covalent than the Sr−O bond. Consequently, the electronic cloud of oxygen atoms is more polarized by Ce than by Sr, and the covalent character of the Ce−O bond is enhanced when Sr^{2+} cations are inserted in the Ce−O network. Thus, the Ce−O bond has a higher ionicity in CeO_2 than in $SrCeO_3$ and Sr_2CeO_4, so the VB−CB separation is greater in CeO_2. In Sr_2CeO_4 this inductive effect is counterbalanced by a split in the O 2p bands. The O_{ap} atom is bonded to one Ce atom, but the O_{eq} atom is bonded to two Ce atoms (Figure 1c), so the 2p orbitals of O_{ap} interact less with the surrounding cations than do those of O_{eq}. Thus, the 2p orbitals of O_{ap} are lowered less in energy than are those of O_{eq}. This explains the splitting in the top of the O 2p-block bands (Figure 4). This band split shifts the band gravity center to higher energy so that the O 2p−Ce 4f gap of Sr_2CeO_4 becomes similar to that of $SrCeO_3$, while the O 2p−Ce 5d gap of Sr_2CeO_4 becomes smaller than that of $SrCeO_3$.

Dielectric Constants. With use of the results of our electronic structure calculations, the imaginary part ϵ_2 of the dielectric function was calculated up to 40 eV. As described in the Experimental Section, the conduction bands positions were raised in energy by a "scissors operator" (0.9 eV) prior to the interband transition strength calculation to match the general features of the measured imaginary part of ϵ.

In Figures 5a, 6a, and 7a, we compare the experimental and calculated isotropic imaginary part of the complex dielectric function for CeO_2, $SrCeO_3$, and Sr_2CeO_4, respectively. Also shown in these plots are the calculated contributions of the O 2p → Ce 4f, O 2p → Ce 5d, and Ce 5p → Ce 5d electronic transitions (see Figure 8). The measured and theoretical curves of $Im(\epsilon)$ are in satisfactory agreement. In the 0−40 eV energy range, the $Im(\epsilon)$ plot exhibits three contributions cen-

(31) Koelling, D. D.; Boring, A. M.; Wood, J. H. *Solid State Commun.* **1983**, *47*, 227−232.
(32) Landrum, G. A.; Dronskowski, R.; Niewa, R.; DiSalvo, F. J. *Chem. Eur. J.* **1999**, *5*, 515522.
(33) Gennard, S.; Furio, C.; Catlow, R. A. *J. Phys. Chem. B* **1999**, *103*, 10158−10170.
(34) Matsumoto, M.; Soda, K.; Ichikawa, K.; Taguchi, Y.; Jouda, K.; Kageyama, M.; Satochi, T.; Sata, N.; Tezuka, Y.; Shin, S.; Kimura, S.; Aita, O. *J. Electron. Spectrosc.* **1996**, *78*, 179−182.
(35) Etourneau, J.; Portier, J.; Ménil, F. *J. Alloys Compd.* **1992**, *188*, 1.

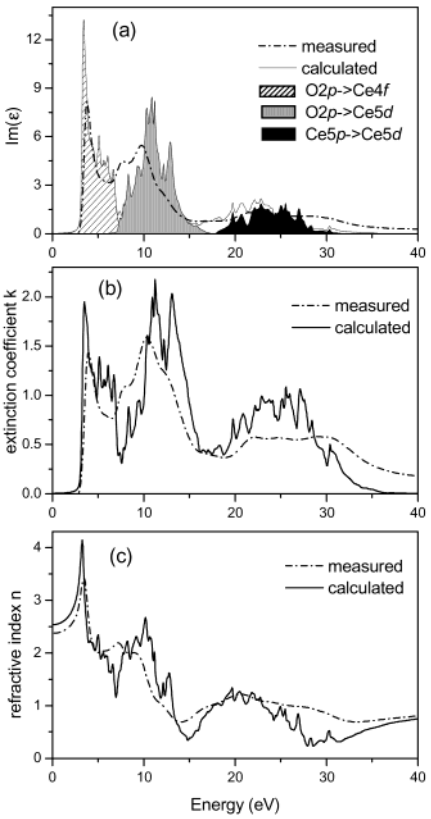

Figure 5. Measured and calculated optical properties of CeO_2: (a) the isotropic imaginary part of the dielectric function, (b) the extinction coefficient *k*, and (c) the refractive index *n*. The contributions of the O 2p → Ce 4f, O 2p → Ce 5d, and Ce 5p → 5d transitions are also given in (a).

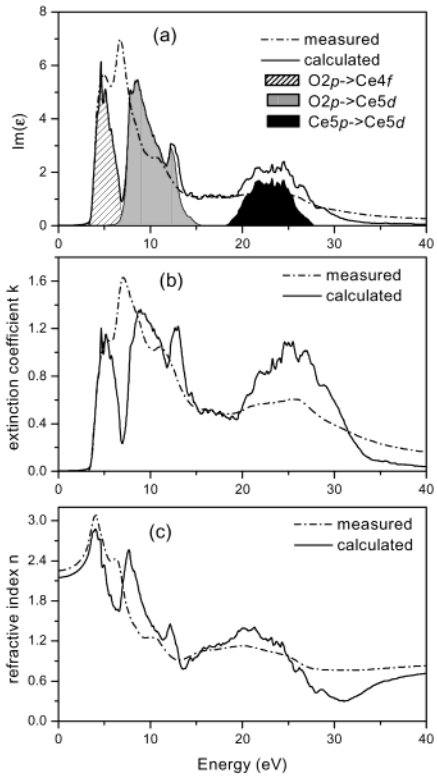

Figure 6. Measured and calculated optical properties of $SrCeO_3$: (a) the isotropic imaginary part of the dielectric function, (b) the extinction coefficient *k*, and (c) the refractive index *n*. The contributions of the O 2p → Ce 4f, O 2p → Ce 5d, and Ce 5p → 5d transitions are also given in (a).

tered around ~6, ~12, and ~25 eV, which are associated with the O 2p → Ce 4f, O 2p → Ce 5d, and Ce 5p → Ce 5d transitions, respectively. The peak decomposition of ϵ_2 allows one to attribute unambiguously the first absorption peak to the O 2p → Ce 4f transition, as asserted by Wuilloud et al.[29] for CeO_2.

From the decomposed $\epsilon_2(E)$ curves, one can calculate the absorption intensity of a given electronic transition upon integration. The absorption intensity associated with the O 2p → Ce 4f transition is weaker for $SrCeO_3$ and Sr_2CeO_4 than for CeO_2 by a factor of 2 and 3, respectively. The corresponding intensity for the O 2p → Ce 5d absorption is weaker for $SrCeO_3$ and Sr_2CeO_4 by a factor of 4/3. These observations can be understood by comparing the oxygen surroundings. The O 2p → Ce 4f transition is associated essentially with the electron excitation from the 2p orbitals of one oxygen to the 4f orbitals of its adjacent cerium atoms. As discussed before, each oxygen atom is surrounded by 4 cerium atoms in CeO_2, 2 in $SrCeO_3$, and 1.5 on average in Sr_2CeO_4; that is, the average number of O−Ce bonds per oxygen is lower for $SrCeO_3$ and Sr_2CeO_4 than for CeO_2 by a factor of 2.0 and 2.7, respectively. The intensity of the O 2p → Ce 4f transition becomes weaker with decreasing the average number of O−Ce bonds per oxygen. Since the surrounding O−Ce bonds can be considered as channels for electron travel, the signal intensity of the O 2p → Ce 4f transition should decrease on going from CeO_2 to $SrCeO_3$ and Sr_2CeO_4. For the O 2p → Ce 5d transition, the decrease in the signal intensity, on going from CeO_2 to $SrCeO_3$ and Sr_2CeO_4, is less pronounced. This is understandable because the covalent character of the Ce−O bond increases on going from CeO_2 to $SrCeO_3$ and Sr_2CeO_4 and because an increased covalent character should be more effective for the O 2p → Ce 5d transition.

The calculated extinction coefficient *k* and refractive index *n* (Figures 5b,c, 6b,c, and 7b,c) are in good agreement with the experimental data, and the shapes of the calculated curves exhibit the same characteristics as do the experimental curves. An interesting feature of the *k* spectra is the shape of the first absorption edge: the stiffness of the slope is greater for CeO_2 than for $SrCeO_3$ and Sr_2CeO_4, thereby allowing for a much steeper absorption of UVA. This feature is related most likely to the high local symmetry of CeO_2. Since all Ce−O bonds are identical, the absorption "bands" from all oxygen atoms are superposed, hence resulting in a sharper peak. An intense UVA absorption seems related to a higher refractive index. For example, the refractive index is largest for CeO_2 ($n = 2.54$) and decreases with increasing the [SrO]/[CeO_2] ratio (i.e., $n = 2.15$ for $SrCeO_3$ and $n = 2.04$ for Sr_2CeO_4). These values are slightly overestimated because the experimental value for CeO_2 is ~2.35. As pointed out above, the real and imaginary parts of ϵ are linked by the Kramers−Kronig relationship:

$$\epsilon_1(0) = 1 + \frac{2}{\pi}\int_0^{+\infty} \frac{\epsilon_2(\omega)}{\omega}\, d\omega$$

Since $\epsilon_1(0) = n_0^2$, the greater n_0 results when the integration of the $\epsilon_2(\omega)/\omega$ terms is larger. The comparison of the calculated and measured curves in Figures

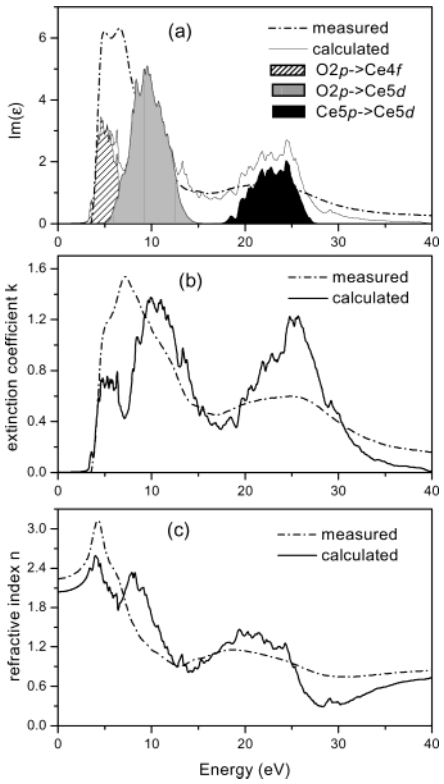

Figure 7. Measured and calculated optical properties of Sr_2CeO_4: (a) the isotropic imaginary part of the dielectric function, (b) the extinction coefficient k, and (c) the refractive index n. The contributions of the O 2p → Ce 4f, O 2p → Ce 5d, and Ce 5p → 5d transitions are also given in (a).

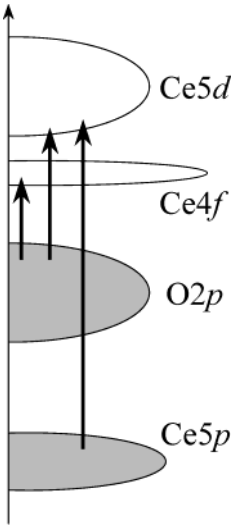

Figure 8. Schematic representation of the three excitations common to CeO_2, $SrCeO_3$, and Sr_2CeO_4.

5a, 6a, and 7a shows that DFT calculations overestimate ϵ_2 intensity mainly at high energies, which leads to a slight overestimation of the n_0 values. In any event, the expected trend, that is, a decrease in n with increasing the [SrO]/[CeO_2] ratio is observed.

From a chemical point of view, the refractive index of a compound is a measure of its polarizability. The Sr−O bond is more ionic than the Ce−O bond, so the overall ionic character is stronger in $SrCeO_3$ and Sr_2CeO_4 than in CeO_2. Thus, the polarizability and hence the refractive index should be lower in $SrCeO_3$ and Sr_2CeO_4 than in CeO_2. This is what is expressed by the Gladstone−Dale formula,[36]

$$n = 1 + \rho \sum_i p_i \times r_i$$

where n is the refractive index, ρ is the density of the complex compound, and p_i and r_i are respectively the weight fraction and the empirically determined refractive coefficient of the constituting binary i. Thus, the refractive index of a complex material can be viewed as the sum of the different contributions of its simple oxide constituents (i.e., CeO_2 and SrO). This reasoning shows that the refractive index should decrease as the Sr content increases since the refractive indices of SrO and CeO_2 are 1.81 and 2.54, respectively.

To summarize, the use of Sr/Ce oxides lowers the transition intensity, the refractive index, and the O 2p−Ce 5d gap. The optical gap is associated with the O 2p−Ce 4f excitation and is influenced by the local environments of the oxygen. This explains why the optical gap energy and n_0 are not related in contradiction to the relationship given by Dimitrov et al.[37] Namely, CeO_2 has a low gap and a high refractive index and $SrCeO_3$ has a high gap and a low refractive index, while Sr_2CeO_4 has a low gap and a low refractive index.

Conclusion

Optical properties of CeO_2, $SrCeO_3$, and Sr_2CeO_4 were measured by means of diffuse reflectance and EELS, and the results were compared and analyzed on the basis of DFT electronic band structure and optical properties calculations. The measured and calculated n, k, and ϵ_2 values are in good agreement. The optical gap was found to be 3.2, 3.5, and 3.2 eV for CeO_2, $SrCeO_3$, and Sr_2CeO_4, respectively. The O 2p → Ce 4f transition is responsible for the first absorption peak and the O 2p → Ce 5d transition for the second absorption peak. An increase in the ionicity of the Ce−O bond widens the O 2p−Ce 5d excitation gap. The decrease in the transition intensity on going from CeO_2 to $SrCeO_3$ and Sr_2CeO_4 was related to the O atom coordination and the Ce−O bond covalency.

Of the three compounds we studied, only CeO_2 presents a proper absorption edge for an UV absorber. This edge is located at the suitable value (3.2 eV) and the absorption peak is steep at the required absorption edge. This is not the case for Sr_2CeO_4, whose absorption peak does not have a steep slope. Therefore, Sr_2CeO_4 is unsuitable for UV absorption applications, although its edge is located at the right energy. For $SrCeO_3$, neither the absorption edge (3.5 eV) nor the steepness of the absorption peak meets the required properties. Thus, $SrCeO_3$ cannot be used for UV absorption applications. For the purpose of UV absorption properties, other compounds should be searched for by considering the influence of the structure and the chemical bonds elucidated in the course of the present study. Such materials should probably have similar cerium coordination to avoid dispersion of the absorption band, and great care should be taken in choosing the extra cations

(36) Newnham, R. *Structure−Property Relations*; Springer-Verlag: Berlin, 1975.
(37) Dimitrov, V.; Sakka, S. *J. Appl. Phys.* **1996**, *79*, 1736−1740.

for ternary phases (A−Ce−O) to avoid unfavorable changes in the ionicity of the Ce−O bonds.

Acknowledgment. The work at Institut des Matériaux Jean Rouxel was supported by Rhodia Electronics and Catalysis, under Grant N2/007070. The work at North Carolina State University was supported by the Office of Basic Energy Sciences, Division of Materials Sciences, U.S. Department of Energy, under Grant DE-FG02-86ER45259.

CM034618U